Protein A/G-based surface plasmon resonance biosensor for regenerable antibody-mediated capture and analysis of nanoparticles

Colloids and Surfaces A: Physicochemical and Engineering Aspects 654 (2022) 130015

Contents lists available at ScienceDirect

Colloids and Surfaces A: Physicochemical and Engineering Aspects

journal homepage: www.elsevier.com/locate/colsurfa

Protein A/G-based surface plasmon resonance biosensor for regenerable antibody-mediated capture and analysis of nanoparticles

Petteri Parkkila [a,b,c,*], Kai Härkönen [d], Petra Ilvonen [d], Saara Laitinen [d], Tapani Viitala [a,b,**]

[a] Drug Research Program, Faculty of Pharmacy, Division of Pharmaceutical Biosciences, University of Helsinki, P.O. Box 56, Helsinki 00014, Finland
[b] Drug Research Program, Faculty of Pharmacy, Division of Pharmaceutical Chemistry and Technology, University of Helsinki, P.O. Box 56, Helsinki 00014, Finland
[c] Department of Physics, Chalmers University of Technology, Gothenburg SE-412 96, Sweden
[d] Finnish Red Cross Blood Service, Kivihaantie 7, Helsinki 00310, Finland

HIGHLIGHTS

- Generic immunocapture biosensor for nanoparticle capture and analysis is presented.
- Size and concentration of the captured nanoparticles are determined using surface plasmon resonance.
- Sensor can be reused multiple times.

GRAPHICAL ABSTRACT

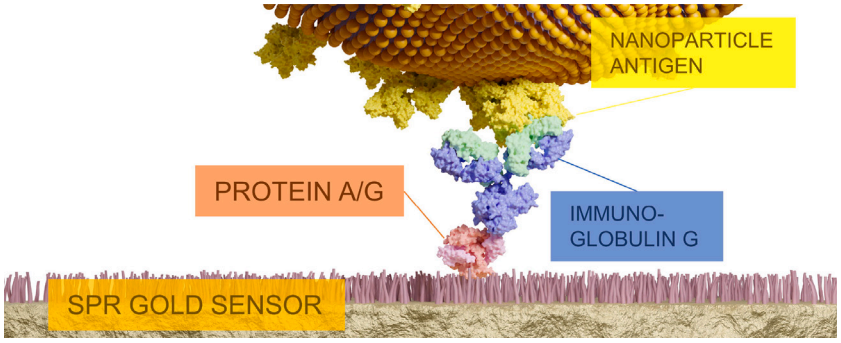

ARTICLE INFO

Keywords:
Nanoparticles
Surface plasmon resonance
Biosensors
Extracellular vesicles

ABSTRACT

Characterization of nanoparticles (NPs) and their subpopulations in heterogeneous samples is of utmost importance, for example, during the initial design of targeted NP therapies and the different phases of their production cycle. Biological NPs such as extracellular vesicles (EVs) have shown promise in improving the drug delivery capabilities compared to traditional NP-based therapies, for example, in treating cancer and neurodegenerative diseases. This work presents a general antibody-mediated surface capture and analysis protocol for NPs using a Protein A/G-functionalized surface plasmon resonance biosensor. The use of anti-streptavidin antibodies allows regenerable capture of biotin-containing NPs such as large unilamellar vesicles commonly used as drug delivery vehicles. Furthermore, the use of antibodies directed against glycophorin A and B (CD235a and b) enabled diffusion-limited specific surface capture of red blood cell-derived extracellular vesicles (RBC EVs). RBC EVs showed the efficacy of the biosensor in the determination of size and bulk concentration of NP subpopulations isolated from a complex biological matrix. The mean size of the surface-captured RBC EVs was comparable to the corresponding sizes derived for the entire EV population measured with well-established NP sizing techniques, namely, nanoparticle tracking analysis and dynamic light scattering. Taken together, the Protein A/G-functionalized biosensor provides a generic alternative to the existing NP-capturing sensors based on, for example, covalent antibody attachment, hydrophobic surfaces or biotin-capped self-assembled monolayers.

* Corresponding author at: Department of Physics, Chalmers University of Technology, Gothenburg SE-412 96, Sweden.
** Corresponding author at: Drug Research Program, Faculty of Pharmacy, Division of Pharmaceutical Chemistry and Technology, University of Helsinki, P.O. Box 56, Helsinki 00014, Finland.
E-mail addresses: petteri.parkkila@chalmers.se (P. Parkkila), kai.harkonen@veripalvelu.fi (K. Härkönen), petra.ilvonen@veripalvelu.fi (P. Ilvonen), saara.laitinen@veripalvelu.fi (S. Laitinen), tapani.viitala@helsinki.fi (T. Viitala).

https://doi.org/10.1016/j.colsurfa.2022.130015
Received 24 May 2022; Received in revised form 13 August 2022; Accepted 18 August 2022
Available online 28 August 2022

1. Introduction

The use of nanoparticles (NPs) in therapeutic applications has shown emerging progress, as evident from the recent success of mRNA vaccines [1]. Their use still faces certain limitations, which can be attributed to the uncertainties in, e.g., mechanisms of their cell internalization [2] and events occurring at the nano-bio-interface [3]. Therefore, efficient in vitro platforms in terms of throughput and reusability for multifunctional studies of NPs to assess their efficacy are in high demand. Label-free methodologies, such as surface-enhanced Raman spectroscopy [4], surface plasmon resonance (SPR) [5–7], waveguide-based scattering microscopy [8], scattered light imaging [9], and novel combinations of techniques such as nanoparticle tracking analysis coupled to asymmetrical flow field flow fractionation [10], and Raman-enabled NP trapping analysis [11], are increasingly gaining traction due to their ability to measure properties such as size, concentration, refractive index, chemical composition, and cell uptake and localization of NPs. Notably, the use of label-free techniques can evade the possible modulation of cellular responses induced by the attachment of fluorescent moieties [12], which, when present on the surface of the NPs, may alter their biological identity.

Extracellular vesicles (EVs) are an important biological subset of lipid-based NPs, which act in intercellular communication. As natural vehicles for molecular transport, their use as carriers of therapeutic cargo have extensively been studied [13,14]. In addition, biomolecular fingerprints of EVs reflects the properties of their parent cells which enables their use as novel biomarkers [15]. From major tissues, blood is a rich source of EVs, as red blood cells (RBCs) vesiculate extensively during their lifespan [16]. The separation of EVs from their biological matrix, however, remains a challenge. A significant hurdle in the preparation of EV-based therapies is the batch-to-batch variations and the heterogeneity of the EVs, in terms of their biophysical properties, such as size and presence of surface protein markers. To this end, the capture of EVs on surfaces can act as an additional purification step for studying diagnostically and therapeutically relevant EV subpopulations. Surface-bound EVs are not prone to interferences from the purification medium and vesicle diffusion or aggregation, which could otherwise influence the downstream characterization or measurements of interactions between EVs and analytes of interest. As a downside, surface-immobilization may induce translational constraints that affect the dynamics of these interactions [17]. In addition, the control of the background signal from non-specific binding to the surface around the immobilized EVs remains a complication if the signals from individual EVs cannot be resolved.

Direct immobilization of antibodies on surfaces using, e.g., amino-reactive cross-linking chemistry, generally does not guarantee the optimal orientation of the bound antibodies [18]. This can be overcome by utilizing Protein A and G, proteins of bacterial origin, commonly used in antibody purification as covalently bound to agarose beads or as bioconjugated NPs [19,20]. Schmid et al. [21] presented a simple protocol for preparing site-directed Protein A-based SPR biosensors using a homobifunctional dithiobis-succinimide-propionate (DSP) crosslinker. Later, other strategies for site-directed immobilization of antibodies have been presented utilizing various Protein A and G variants [22,23], which, however, are not readily available for laboratories without facilities for protein production. In contrast to these studies, we pursued to have a more general system based on commercially available reagents. Based on the work of Schmid et al. [21], we hypothesized that Protein A/G, a recombinant fusion protein containing immunoglobulin (IgG) Fc region binding domains from both Protein A and Protein G [24], could be utilized in the preparation of SPR antibody-capturing sensors instead of Protein A to support studies with a wider range of IgG subclasses. Furthermore, instead of using the prepared sensors for immunoassay applications, our aim was to use the Protein A/G sensors in combination with dual-wavelength surface plasmon resonance detection to determine the size and concentration of captured NPs, such as biotinylated vesicles and specific subpopulation of RBC-derived EVs. The conventional capturing protocols for NPs require specific surface chemistries for different types of particles, e.g., positively charged sensors for viruses [25] and biotin-functionalized sensors for streptavidin-mediated NP capturing [26]. These surface chemistries, however, leads to practically irreversible binding of the NPs and the regeneration of the sensor surfaces for repeated capture cycles is challenging, consequently increasing the number of sensors needed, and thus, the costs of the NP assay.

In order to address the need for regenerable and generically applicable nanoparticle analysis platforms, we present in this work an optimized protocol for the preparation of Protein A/G biosensors. Sensors can be prepared in-house on non-functionalized gold sensors, making them a cost-effective solution for the studies of NPs bearing any surface antigens. The sensor also functions as a re-generable biotin-capturing sensor when using an anti-streptavidin antibody as an intermediate streptavidin binding agent. So far, the use of regenerable biotin-capturing sensors have been limited to specifically designed proprietary avidin mutants which reversibly bind to biotin [27]. As a proof-of-concept, we demonstrate in this work the use of the Protein A/G sensor with lipid-based nanoparticles, namely, synthetic large unilamellar vesicles (LUVs) and RBC-derived EVs. Finally, we utilize the formalism developed by Rupert et al. [5,6] for the simultaneous determination of the size and bulk concentration of the vesicles, showing the use of the sensor in multiparametric NP screening and characterization.

2. Materials and methods

2.1. Chemicals

Protein A from *Staphylococcus aureus* (P7837), bovine serum albumin (05482), dimethyl sulfoxide (276855), monoethanolamine (E9508), (3-aminopropyl)triethoxysilane (440140), glycine (33226), 2-propanol (34863), hydrogen peroxide (95321) and ammonium hydroxide (221228) were obtained from Sigma-Aldrich (St. Louis, MO, USA). 1,2-dipalmitoyl-*sn*-glycero-3-phosphocholine (850355P, DPPC), 1,2-distearoyl-*sn*-glycero-3-phosphoethanolamine-*N*-[methoxy(polyethylene glycol)-2000] (880120P, DSPE-PEG2k) and 1,2-distearoyl-*sn*-glycero-3-phosphoethanolamine-*N*-[biotinyl(polyethylene glycol)-2000] (880129P, DSPE-PEG2k-Biotin) were obtained from Avanti Polar Lipids (Alabaster, AL, USA). Recombinant Protein A/G (77677, product of Pierce), streptavidin (434301), dithiobis(succinimidyl propionate) (22585) and 0.1 μm sulfate latex beads (S37204) were purchased from Thermo Fisher Scientific (Rockford, IL, USA). Purified anti-streptavidin (410501, Clone: 3A20.2, Isotype: Mouse IgG2b, κ), purified anti-human CD235ab (306602, Clone: HIR2, Isotype: Mouse IgG2b, κ), purified anti-human CD41 (303702, Clone: HIP8, Isotype: Mouse IgG1, κ) and purified anti-human CD235a antibodies (349102, Clone: HI264, Isotype: IgG2a, κ) were produced by BioLegend (San Diego, CA, USA). Chemicals from other manufacturers include Triton X-100 (807423) from MP Biomedicals (Irvine, CA, USA), 99.5% (w/w) ethanol from Altia Oyj (Helsinki, Finland) and xylitol (no product code available) from Danisco (Copenhagen, Denmark). Phosphate-buffered saline (PBS) was produced with a following recipe in 1 liter batches: 8.0 g of sodium chloride (31434) from Honeywell Riedel-de Haën (Seelze, Germany), 0.2 g of potassium chloride (31248) from Honeywell Riedel-de Haën, 1.4 g of sodium phosphate dibasic dihydrate (0326) from J.T. Baker (Phillipsburg, NJ, USA) and 0.2 g of monopotassium phosphate (4871) from Merck (Darmstadt, Germany). Ion exchanged water from a Milli-Q purification system (Merck) was used in all sample preparations.

2.2. Sample preparation

2.2.1. LUV preparation

LUVs with a lipid composition DPPC:DSPE-PEG2k:DSPE-PEG2k-Biotin (96:3.5:0.5 molar ratio) were prepared by thin-film evaporation method. Briefly, lipids were mixed from their chloroform stock solutions, and chloroform was evaporated at reduced pressure using a rotavapor system with a 60 °C water bath. The lipid film was dissolved in 1 mL of PBS (5 mg/mL total lipid concentration), and the test tube was vortexed vigorously with brief incubations in the water bath to maintain the temperature. Vesicles were diluted to the concentration of 2.5 mg/mL and extruded 11 times through a 100 nm filter device (T&T scientific, Knoxville, TN, USA) or 400 nm filter membrane (Avanti Polar Lipids) at 60 °C. Vesicle solutions were cooled and stored at 4 °C until use.

2.2.2. RBC EV preparation

Leukocyte-reduced erythrocyte concentrates from Finnish Red Cross Blood Service were used as starting material for RBC EV isolation. Concentrates were handled anonymously, and only concentrates that could not be administered clinically were used as accepted by the Finnish Supervisory Authority for Welfare and Health (Valvira, Finland). RBC EVs were isolated based on the protocol described by Valkonen et al. [28]. First, erythrocyte concentrates were diluted 1:1 with cold calcium and magnesium chloride-free 1 × Dulbecco's phosphate-buffered saline (DPBS) (A12856-01, product of Gibco, Thermo Fisher Scientific) and centrifuged for 10 min at 800 × g at room temperature (RT) without brake (Rotor A-4-81, Eppendorf Centrifuge 5810R). Supernatant was transferred to new tubes. The erythrocyte pellet was resuspended ad. 50 mL to cold DPBS and centrifuged for 20 min at 1560 × g, RT without brake. The supernatant was combined with supernatant from the previous centrifugation step. The supernatant was centrifuged for 20 min at 3000 × g, RT with brake (brake setting 9). The supernatant was transferred to Optiseal ultracentrifuge tubes (361625, Beckman Coulter, CA, USA) and centrifuged for 60 min at 100 000 × g, 4 °C (Rotor MLA-50, Optima MAX-XP ultracentrifuge, Beckman Coulter). Supernatants were discarded, and pellets were resuspended in DPBS and transferred to Ultra-Clear centrifuge tubes (344057, Beckman Coulter) and centrifuged for 90 min at 100 000 × g, 4 °C (Rotor MLS 50, Optima MAX-XP ultracentrifuge, Beckman Coulter). The obtained pellets were suspended in cold DPBS and stored at −80 °C. Protein concentration of the RBC EVs was measured using DC (detergent compatible) Protein Assay Kit II (5000112, Bio-Rad, Hercules, CA, USA) as per the instructions of the manufacturer in the presence of 0.5% (w/v) Triton X-100.

2.2.3. General protocol for sensor preparation

Gold sensor slides (BioNavis, Tampere, Finland) were first cleaned in a boiling solution of water, hydrogen peroxide and ammonium hydroxide (5:1:1 volume ratio) for 5 min, flushed with 70% (v/v) ethanol and water, and dried with nitrogen flow. Then, the background SPR spectra of the sensors were measured in PBS for 5 min. Sensors were flushed with water and cleaned using oxygen plasma at 29.6 W and 133–173 Pa (PDC-002, Harrick Plasma, Ithaca, USA) for 5 min. Sensors were immediately immersed in a 10 mM solution of DSP in dimethyl sulfoxide (DMSO) for 30 min. Protein A or A/G were dissolved in PBS with the concentration of 1 mg/mL, sterile filtered through a 0.2 μm membrane, and stored at −20 °C in 0.5 mL aliquots until use. Sensors were immersed in DMSO and PBS and incubated in 0.5 mg/mL of Protein A or A/G solutions overnight (16–20 h). The remaining reactive sites were blocked using a 30-minute incubation in 1 M monoethanolamine (MEA), pH 8.6. The sensors were then incubated for 15 min in 10 mg/mL solution of bovine serum albumin (BSA) in PBS followed by a 5-minute incubation in 0.2 M glycine–HCl (pH 2.5) and stored in PBS at 4 °C until use. Sensors were immersed in PBS between all incubations. The incubations were performed at room temperature except for the incubation in Protein A or A/G solutions, which was performed at 4 °C. Sensors were reused three times (initiated by the initial cleaning protocol) in the experiments where the preparation conditions were varied, although a different sensor was always used for each condition. For the calibration experiment using polystyrene beads, (3-aminopropyl)triethoxysilane (APTES) functionalization was performed by first cleaning a SiO_2 sensor (BioNavis) using oxygen plasma and then placing the sensor in the mixture of 160 μl of APTES and 2 mL of IPA for 4 h. The sensor was flushed with IPA, dried under nitrogen flow, and stored at 4 °C until use.

2.3. Surface plasmon resonance

A multi-parametric dual-wavelength (670 and 785 nm) surface plasmon resonance instrument (MP-SPR Navi 220 A, Bionavis) with two parallel flow channels was used in the experiments (20 °C, flow rate of 20 μl/min). In each run, 5-minute injection of 300 mM xylitol in PBS was used for the calibration of the sensitivity coefficients of the sensor. Surface was regenerated using injections of 0.2 M glycine–HCl (pH 2.5) mixed with isopropanol (1:1 v/v, later referred to as glycine–HCl–IPA) (LUVs) or 0.5% (w/v) Triton X-100 followed by glycine–HCl–IPA (RBC EVs). Geometry factors needed for the bulk concentration calculations were determined using polystyrene beads with a concentration of 10 μg/mL in water.

2.4. Nanoparticle tracking analysis and dynamic light scattering

Concentrations and size distributions of particles in LUV (stored at 4 °C) and RBC EV (freezed aliquots) samples were measured using nanoparticle tracking analysis (NTA, Nanosight LM14C, Malvern Instruments Ltd., Malvern, UK). 3 × 60 s (LUVs) or 5 × 30 s (RBC EVs) videos were taken with camera level 16, detection threshold 5, blue laser: 405 nm, 60 mW, and using software version 3.4, builds 3.4.003 (LUVs) and 3.4.4 (RBC EVs). Optimal dilution for measurements was obtained by diluting the samples with PBS to achieve concentrations of 20–100 particles per frame as recommended by the instrument manufacturer. Dynamic light scattering (DLS) experiments were performed using an automated Zetasizer APS instrument (Malvern Instruments Ltd, Worcestershire, UK) with dilutions of 0.5 mg/mL for the LUVs and 4×10^{10} particles/mL for the RBC EVs.

2.5. Determination of vesicle sizes and surface coverages from SPR measurements

A general equation for the SPR response (R, change in the SPR peak angle minimum in degrees) for an arbitrary particle on the sensor surface can be written as

$$R = S\left(\mathrm{d}n/\mathrm{d}C_*\right) c_* c \nu_\mathrm{p} \delta^{-1} \varphi(d,\delta), \tag{1}$$

where S = sensor sensitivity coefficient, $\left(\mathrm{d}n/\mathrm{d}C_*\right)$ = refractive index increment of the molecules forming the particle (units of mL/g), c_* = concentration of molecules forming the particle (units of g/mL), c = number of particles per unit area (units of cm^{-2}), ν_p = integral volume occupied by molecules forming the particle (units of mL), δ = decay length of the SPR evanescent field (units of cm), φ = dimensionless factor that takes into account the integral volume of the particle in relation to the SPR evanescent field and depends on the decay length δ and particle diameter d [6]. Capital C throughout this work refers to bulk concentrations, as per notation introduced by Rupert et al. [6]. Subscript '*' refers to concentrations of molecules in the particle as opposed to concentrations of particles.

Since SPR responses depend on the used wavelength and the physical properties of the sensor, in any applications of SPR, it is desired to write Eq. (1) in terms of surface-mass density representing the adsorbed mass of particles per unit area, $\Gamma = c_* c \nu_\mathrm{p}$ (units of $\mathrm{g/cm}^2$ or $\mathrm{ng/cm}^2$):

$$\Gamma = \frac{\delta R}{S\left(\mathrm{d}n/\mathrm{d}C_*\right)\varphi}. \tag{2}$$

Table 1
Results from the optimization of the conditions for sensor preparation (mean ± S.D.). Mean response for DSP (10 mM, 0.5 h) is subtracted from the data for Protein A/G and Protein A.

		SPR response (°)	Surface-mass density (ng/cm^2)	θ/θ_{RSA} (%)	θ/θ_{RSA} (%) for antibody	Antigen-to-antibody ratio (%)
DSP	2 mM, 0.5 h	0.09 ± 0.05	42 ± 22	43 ± 23		
	2 mM, 1.5 h	0.17 ± 0.04	81 ± 20	84 ± 21		
	10 mM, 0.5 h	0.18 ± 0.02	88 ± 11	92 ± 12		
Protein A/G	0.5 mg/mL, 2 h	0.22 ± 0.15	102 ± 72	43 ± 30	51 ± 1	66 ± 1
	1 mg/mL, 2 h	0.17 ± 0.07	78 ± 33	33 ± 14	54 ± 12	66 ± 2
	0.5 mg/mL, 18 h	0.19 ± 0.07	92 ± 35	39 ± 15	42 ± 5	63 ± 7
	on plain gold	0.44 ± 0.09	225 ± 62	94 ± 26	20 ± 13	39 ± 16
	on MEA after DSP	0.14 ± 0.08	67 ± 37	28 ± 16	23 ± 14	72 ± 54
Protein A	0.5 mg/mL, 2 h	0.29 ± 0.15	139 ± 71	62 ± 32	12 ± 2	47 ± 8
	1 mg/mL, 2 h	0.34 ± 0.13	161 ± 60	72 ± 27	16 ± 2	76 ± 15
	0.5 mg/mL, 18 h	0.35 ± 0.01	164 ± 5	73 ± 2	15 ± 2	64 ± 19

Since surface-mass densities do not depend on the used wavelength, dual-wavelength SPR (λ_1 = 670 nm, λ_2 = 785 nm, in our case) can be utilized to determine the size (d = diameter) of the nanoparticle by dividing the set of equations (Eq. (1)) for the two wavelengths [6]:

$$\frac{R_{\lambda_1}}{R_{\lambda_2}} = \frac{S_{\lambda_1}}{S_{\lambda_2}} \frac{\left(\mathrm{d}n/\mathrm{d}C_*\right)_{\lambda_1}}{\left(\mathrm{d}n/\mathrm{d}C_*\right)_{\lambda_2}} \frac{\delta_{\lambda_2}}{\delta_{\lambda_1}} \frac{\varphi\left(d, \delta_{\lambda_1}\right)}{\varphi\left(d, \delta_{\lambda_2}\right)}. \tag{3}$$

Another approach to quantify the coverage of particles on the surface is to define surface coverage (θ), i.e., the fraction of area on the surface occupied by N particles:

$$\theta = \frac{N A_\mathrm{p}}{A} = c A_\mathrm{p}, \tag{4}$$

where A_p is the area of the particle projected on the plane of the sensor surface (for spheres, $A_\mathrm{p} = \frac{1}{4}\pi d^3$ and A is the total surface area of the sensor. Insertion of Eqs. (1) and (2) to Eq. (4) gives the relationship between the surface-mass density and surface coverage:

$$\theta = \frac{\Gamma}{\Gamma_{max}}, \tag{5}$$

where $\Gamma_{max} = c_* v_\mathrm{p}/A_\mathrm{p}$. In this work, we use the relative surface coverage, i.e., the surface coverage of the particles (θ) divided by the saturation coverage of spheres on a surface according to the random sequential adsorption (RSA) model (θ_{RSA} = 54.7%). Therefore, the values are reported as relative surface coverages, i.e., θ/θ_{RSA} with units of %. The values of Γ_{max} differ depending on the particles forming the adsorbed film. These are presented in Supplementary material Eqs. S1–S3.

3. Results and discussion

3.1. Enhancement of the sensor preparation protocol

First, we investigated how the changes in incubation time and bulk concentration of the homobifunctional DSP crosslinker affect the surface coverage of DSP on the gold coated SPR sensor surface (Table 1). The use of 10 mM DSP instead of 2 mM (with the same incubation time) used by Schmid et al. [21] or prolongation of the incubation time resulted in two times higher surface coverages of DSP (Table 1, rows 1–3). This is in agreement with a previous study on self-assembled DSP on gold by Suherman et al. Therefore, 10 mM of DSP with an incubation time of 30 min was used as the basis for all subsequent sensor functionalizations.

Next, the incubation time and concentration of Protein A/G or Protein A were varied (Table 1, rows 4–6 and 9–11), and the binding of an anti-streptavidin antibody and streptavidin was measured in each case. Relative surface coverages were, in general, ca. 2 times higher for Protein A (62%–73%) compared to Protein A/G (33%–43%, Table 1, column θ/θ_{RSA}). The binding capacity of Protein A for the anti-streptavidin antibody, however, was considerably lower (12%–16%) compared to Protein A/G (42%–54%, Table 1, column θ/θ_{RSA} for antibody). For Protein A/G sensors, approximately every two out of three antibody molecules bind streptavidin (63%–66%, Table 1, column Antigen-to-antibody ratio), which suggests that the antibodies are well-oriented on the surface. In addition, incubation of 0.5 mg/mL Protein A/G on plain gold revealed that the protein becomes fully packed on the surface relative to the jamming limit (94%), but the relative surface coverage of the anti-streptavidin antibody was reduced to approximately half (20%) compared to the site-directed immobilization with Protein A/G (Table 1, row 7). A similar reduction for the relative surface coverage of the anti-streptavidin antibody was observed if the reactive N-hydroxysuccinimide (NHS) esters of DSP were deactivated using monoethanolamine (MEA, Table 1, row 8). The effects of changing incubation time and protein concentration on the relative surface coverages determined for both Protein A and Protein A/G immobilization were negligible. However, the variation between the three repeat measurements for Protein A when using the overnight incubation was clearly smaller compared to the shorter incubation time (Table 1, column θ/θ_{RSA}). Consequently, and due to the fact that overnight incubation was the recommended protocol in the original study of Schmid et al. [21] for Protein A sensor preparation, we opted to use an overnight (16–20-hour) incubation time for Protein A/G in subsequent experiments. The optimized Protein A/G sensor preparation protocol is schematically presented in Fig. 1.

Fig. 2 shows the comparison of the binding kinetics and surface coverage of different IgG subclasses on the Protein A/G sensor. The binding for the IgG1 subclass was generally low with an average relative surface coverages of 27% in terms of the fraction of the jamming limit when comparing to the corresponding average relative surface coverages for IgG2 subclasses, which were in the range of 45%–68%. This reflects the higher capacity of IgG2 subclass antibodies to bind to Protein A/G. The SPR responses in Fig. 2 also demonstrates that the Protein A/G surface can be almost completely saturated in less than five minutes of injection with the antibody concentrations used. The degree of dissociation, on the other hand, varies slightly between the IgG subclasses. Hence, it is beneficial to wait for a sufficiently long time between the end of the antibody injection and the start of the NP capturing in order to minimize the effect of antibody dissociation on the SPR response during NP capturing.

3.2. Surface capture of LUVs and RBC EVs

The efficacy of the prepared Protein A/G sensors for NP capturing were assessed by six sequential injections with increasing bulk concentrations for LUVs, and two different bulk concentrations for RBC EVs (Fig. 3, Supplementary material Figures S3–S8 and S10–S15). As expected, the slope of the SPR response for the LUVs increases with increasing bulk concentration until the jamming limit of the surface (54.7%) is approached. The binding of RBC EVs at a bulk concentration of 4×10^{10} particles/mL was low compared to the concentration of

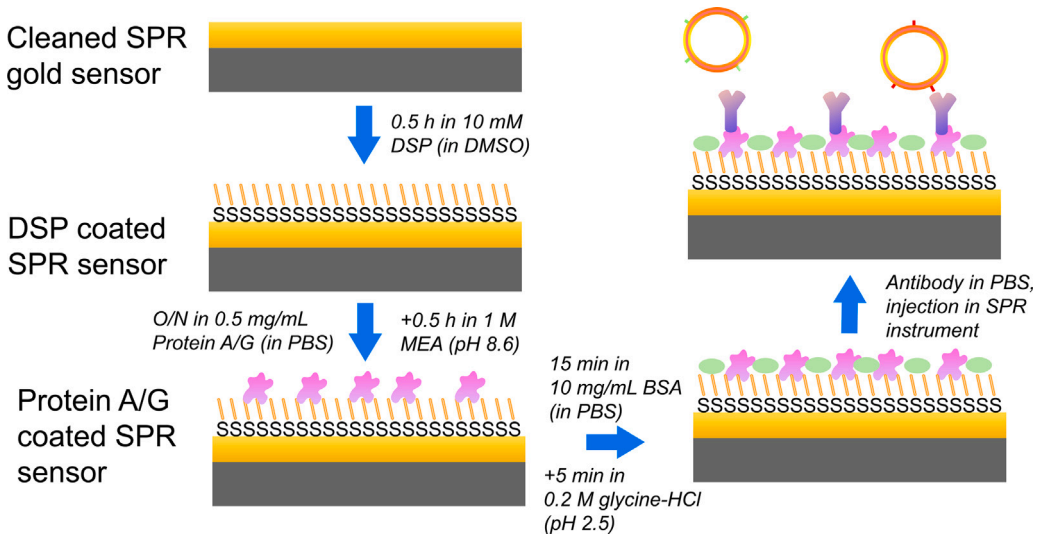

Fig. 1. Schematic representation of the optimized Protein A/G sensor preparation protocol.

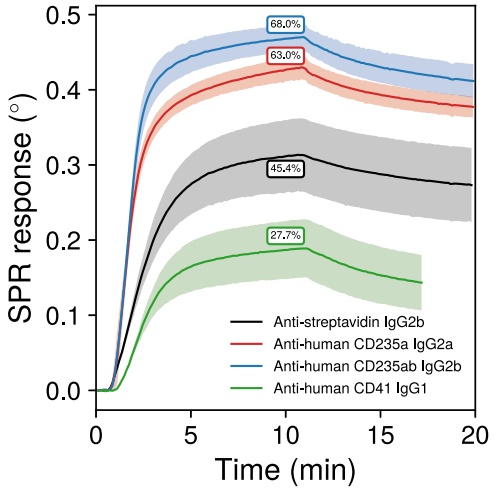

Fig. 2. SPR responses during binding of different IgGs (IgG2a, IgG2b, and IgG1) on the Protein A/G sensor (N = 3 ± S.D.), Percentage values in the boxes indicate mean surface coverages of antibodies relative to the jamming limit (θ/θ_{RSA}). The concentrations used were 10 μg/mL for the anti-streptavidin antibody and 25 μg/mL for other antibodies.

3×10^{11} particles/mL. Since a 10-minute injection time at the flow rate of 20 μl/min was used in the measurements, the sample consumption of this SPR surface capturing technique is relatively high. Non-specific binding of LUVs and RBC EVs, however, were generally low relative to the binding in the presence of antibodies (dashed lines in Fig. 3, Supplementary material Figures S9, S16 and S17). This indicates that the binding of these NPs is due to the specific interactions with the bound antibodies. Therefore, the number of EVs positive in respect to the specific antibody is the determining factor of the capturing efficiency rather than the absolute EV bulk particle concentrations measured using, e.g., NTA. Thus, in comparison with NTA, the factor determining variations in the rate of binding in the SPR assay is the concentration of EVs that are positive for the specific antibody. A means to determine nanoparticle size by utilizing the ratio of the SPR signal responses at two different wavelengths and the nanoparticle bulk concentration from the rate of binding is described in the next sections.

In view of the regeneration of the sensor for consecutive measurements, our preliminary tests with RBC EVs revealed that the sensors could not be regenerated using glycine–HCl–IPA alone. Therefore, an additional regeneration step with Triton X-100 was added before glycine–HCl–IPA to solubilize the EVs. This protocol for sensor regeneration allowed for at least five identical cycles of vesicle capture (Supplementary material Figures S1, S18–S22). In addition to the full regeneration of the sensors by the removal of the antibodies from the surface, we investigated the use of Triton X-100 only for regeneration without the need for recapturing antibodies. Interestingly, the last injection of LUVs when using only Triton X-100 for regeneration resulted in a markedly lower maximum SPR response compared to the first four injections. This was probably due to the partial removal or restructuring of the intermediate streptavidin layer. On the other hand, the most significant decrease in the maximum SPR response for RBC EVs was observed after the first capturing cycle. There is a possibility that trace amounts of Triton X-100, when not removed using glycine–HCl–IPA, can remain on the surface along with solubilized membrane fragments, which diminish the binding of vesicles due to the limited available number of binding sites on the surface. Finally, when the binding of the CD235ab antibody was tested on sensors stored for two weeks in PBS at 4 °C, only a slight decrease in the maximum SPR response (16.7 ± 5.4%) was observed.

3.3. Determination of size of LUVs and RBC EVs

Since the formalism based on dual-wavelength SPR developed by Rupert et al. [6] allows direct measurement of particle size of NPs captured on the sensors, it was of interest to compare the calculations using SPR measurements with the hydrodynamic particle diameters measured by NTA and DLS (Fig. 4). For 200 nm LUVs, a drastic decrease in particle diameter calculated from SPR measurements is evident when the jamming limit is approached. An explanation for this behavior could be the deformation of vesicles [6,30], which would not be as prominent phenomena for EVs that are more rigid compared to LUVs. Both NTA and DLS measurements show that the peak of the size distribution for 200 nm LUVs is around a diameter of ca. 150 nm, which suggests that a considerable number of vesicles have a hydrodynamic size smaller than the mean value of ca. 200 nm. The decreasing diameter for the individually calculated particle size from SPR measurements for the last two LUV injections (25 μg/mL and 100 μg/mL) for both LUV samples suggests that smaller vesicles are favored for binding due to the limited available surface area when the jamming limit is approached. Repeated injection cycles using high concentration of vesicles (100 μg/mL) indeed showed rather low mean diameters calculated from SPR measurements, which highlights the importance, in our case, to operate the SPR-based NP size determinations with

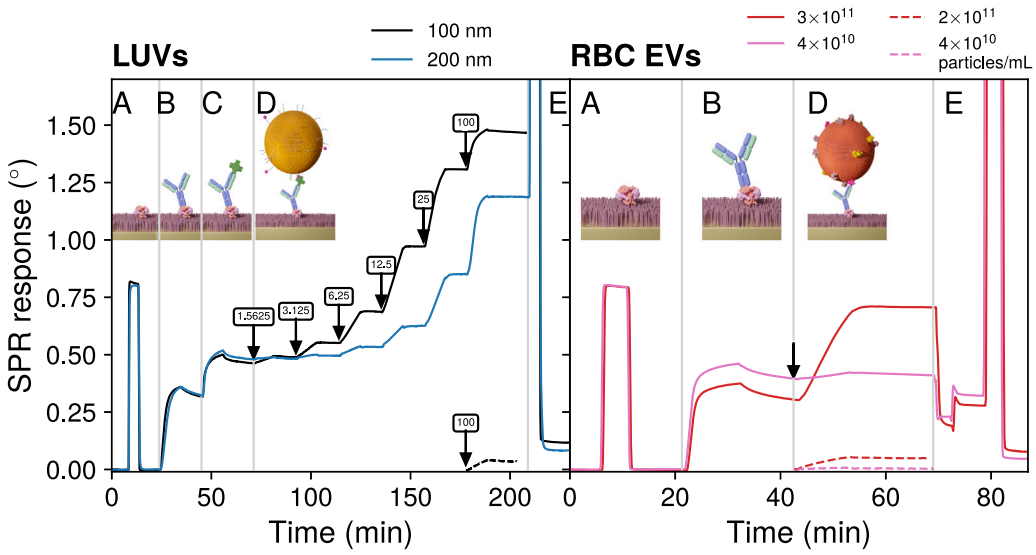

Fig. 3. SPR responses (670 nm wavelength) of measurements with LUVs and RBC EVs (first experiments shown from $N = 3$ measurements). (A) 300 mM xylitol for calibration, (B) 10 μg/mL of anti-streptavidin antibody (LUVs) or 25 μg/mL of anti-CD235ab antibody (RBC EVs), (C) 25 μg/mL of streptavidin (LUVs only), (D) LUVs (C_m = 1.5625, 3.125, 6.25, 12.5, 25 and 100 μg/mL) or RBC EVs ($C_\#$ = 4×10^{10} and 3×10^{11} particles/mL), (E) regeneration using glycine–HCl–IPA (LUVs) or 0.5% (w/v) Triton X-100 and glycine–HCl–IPA (RBC EVs). Vesicle additions are marked by arrows. Bulk concentrations (C_m) of LUV injections are presented in units of μg/mL of lipids. Dashed lines show the responses without antibodies ($C_\#$ = 4×10^{10} and 2×10^{11} particles/mL for RBC EVs).

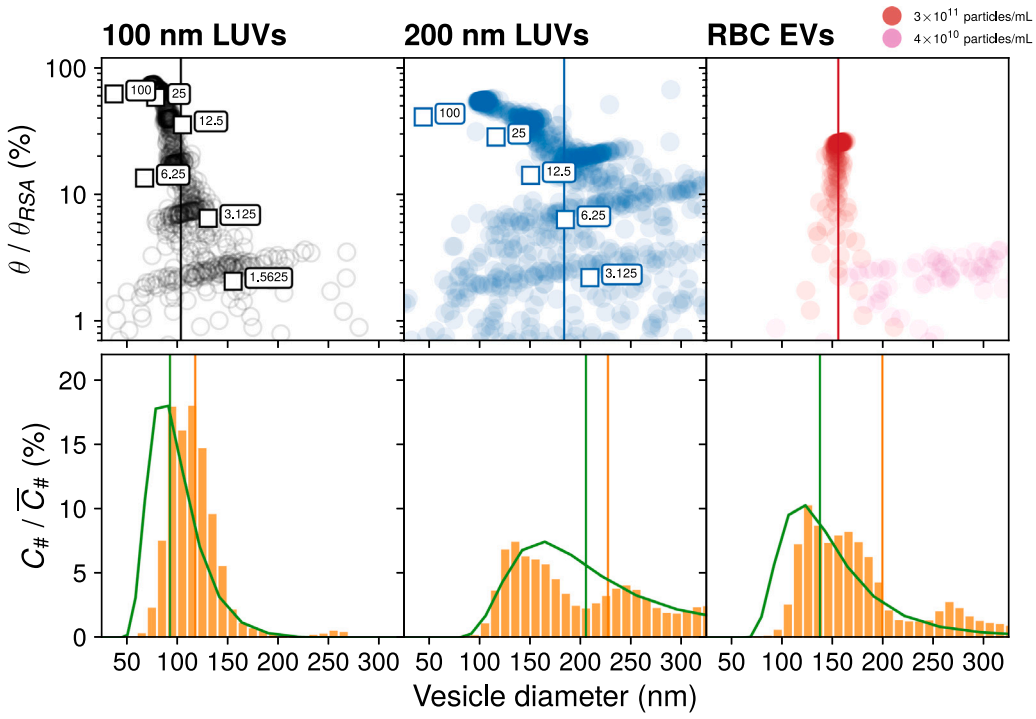

Fig. 4. The top panel shows the dependence of the vesicle diameter measured using SPR on the surface coverage of vesicles relative to the jamming limit (θ/θ_{RSA} in logarithmic scale, mean of $N = 3$ measurements). Squares mark the mean diameters for the individual LUV injections (bulk concentrations shown in the units of μg/mL of lipids). For RBC EVs, surface coverages are shown for bulk concentrations of 4×10^{10} and 3×10^{11} particles/mL. The bottom panel shows the hydrodynamic vesicle diameter distributions in terms of the particle concentration $C_\#$ divided by the mean total particle concentration $\overline{C}_\#$ measured using NTA (orange bars). Green lines depict the corresponding distributions measured using DLS normalized with the maximum of the NTA size distribution data. Vertical lines show the distribution means.

moderate relative surface coverages ($\theta/\theta_{RSA} \approx$ 10%–30%). Also, too low surface coverages raise uncertainties in the size determination, as evident from the large dispersion of data in Fig. 4.

Table 2 further compares the determination of mean vesicle diameters using the SPR, NTA, and DLS techniques. For SPR, vesicle diameters at relative surface coverages (θ/θ_{RSA}) between 20%–25% were first averaged, and then the mean vesicle diameters were determined from three technical replicates. Interestingly, despite the similarities in the size distributions between the 200 nm LUVs and RBC EVs, the former had considerably higher deviation in the diameter at equal surface coverages. This can be partly attributed to the nature of the serial injection experiment performed for the LUVs, where a larger dispersion in the vesicle sizes with increasing bulk concentrations for each injection can be expected due to the longer timescale of the experiment. Interestingly, the mean size for RBC EVs determined by SPR is much closer to the size derived by using DLS than NTA. This may reflect

Table 2
Comparison of different methods for determining the mean vesicle size. Values represent the mean ± S.D. for $N = 3$ independent size measurements for the same sample, except for the NTA data of RBC EVs, for which $N = 5$.

	SPR (nm)	NTA (nm)	DLS (nm)	Polydispersity Index
100 nm LUVs	98.0 ± 14.1	117.9 ± 1.4	92.9 ± 6.7	0.04 ± 0.03
200 nm LUVs	206.9 ± 95.8	226.8 ± 7.7	205.0 ± 20.1	0.17 ± 0.01
RBC EVs	152.3 ± 1.86	198.6 ± 7.4	136.7 ± 11.3	0.23 ± 0.07

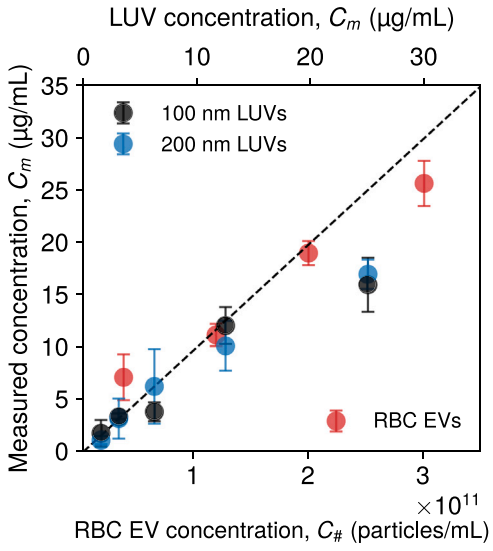

Fig. 5. Measured bulk concentration of particles C_m as a function of the LUV concentration C_m and RBC EV concentration $C_\#$ ($N = 3$ ± S.D.). Data for RBC EVs, where $C_\# = 1.2\times10^{11}$ and 2×10^{11} particles/mL, is derived from the first three injections of the regeneration experiments presented in Supplementary material Figure S1.

the fact that the size determination in NTA is based on diffusion coefficients measured for individual particles, while SPR and DLS are based on ensemble-averaging of the SPR responses in the evanescent field, and scattered light of the EVs, respectively. Alternatively, since DLS is not well suited to study polydisperse nanoparticle samples such as EVs [31], a smaller particle size derived using SPR compared to NTA may reflect a lower mean diameter of the subpopulation of particles captured on the SPR sensor surface.

3.4. Determination of bulk concentration of LUVs and RBC EVs

Since the SPR measurements are performed under global diffusion-limited conditions, which is evident from the LUV titration experiment, the slope of the SPR response can be utilized to calculate the bulk concentration of particles in the sample (Fig. 5, see also Supplementary material Eq. S4) [5,6]. In brief, the bulk concentration of the vesicles is proportional to the rate of binding and the diffusion coefficient, which was determined by using the vesicle diameters derived from the SPR experiments. The protein concentration of RBC EVs solubilized with Triton X-100 was measured to be 7.18 ± 0.15 mg/mL, which translates to 8.25×10^{-16} grams of protein per particle and is comparable with 2.36×10^{-16} grams/particle reported by Koponen et al. [32]. When using the linear relationship between the particle number concentration $C_\#$ measured by NTA and the measured bulk mass concentration C_m (Fig. 5, correlation coefficient $(\Delta C_m)/(\Delta C_\#) = 7.36\times10^{-11}$ μg/particle) results in an estimation that ~9% of the RBC EVs are CD235ab-positive. This result is similar to the value of 21% of CD235a-positive RBC EVs previously reported by Valkonen et al. [28]. Especially, when considering batch-to-batch variations, differences in antibodies, and the uncertainties in the correlation between total protein mass and total mass of EV particles in the sample [6]. The effects of possible blood protein contaminants on this estimate are also unknown. The linear relationship between the actual LUV mass concentration and concentration determined by SPR does not hold after the 25 μg/mL injection of vesicles. This indicates that the surface becomes saturated with vesicles, and thus, the rate of change in the SPR response may not accurately reflect the bulk concentration of the vesicles in that regime of surface coverage.

4. Conclusions

In this work, we have demonstrated antibody-mediated capture protocols for synthetic and biological nanoparticles by functionalizing SPR gold sensors with recombinant Protein A/G. During the enhancement of the preparation protocol of the sensors, we found that an increase in the DSP cross-linker concentration with a constant incubation time leads to increased surface coverage of the cross-linker. The use of Protein A/G instead of Protein A in the sensor preparation increased the binding ability and surface coverage of IgG2b subclass antibodies, although the surface coverage for Protein A/G covalently attached to the DSP cross-linker was lower than for Protein A. The surface capture of synthetic vesicles and red blood cell-derived extracellular vesicles by the Protein A/G sensor demonstrated that the achieved surface coverage of vesicles is linearly proportional to the bulk concentration. To this end, an estimation of the relative abundance of the captured EV subpopulation could be performed together with the size determination utilizing dual-wavelength SPR. Furthermore, regeneration of the biosensor surface allowed multiple capturing cycles either by detergent-assisted removal of vesicles from the surface or complete regeneration by removing the antibodies using a mixture of glycine–HCl and isopropanol.

To conclude, the main advantages of the developed Protein A/G biosensor include ease of preparation and regenerability combined with low non-specific binding, which would be expected to be more prominent given the source of the EVs used in our study. In the future, we envision broadening the use of the Protein A/G sensors for the parallel capture of specific subpopulations of blood-derived EVs using SPR instrumentation with multiple flow channels. In addition, supplementary post-capture antibody injections may be utilized to assess the presence of additional surface biomarkers of EVs and other NPs. Other beneficial uses of the Protein A/G sensor include for example quality control and characterization of EVs during different stages of EV purification or evaluating the purity of EV end products, which is of importance when EV-based therapeutic applications are to be transferred into clinical use.

CRediT authorship contribution statement

Petteri Parkkila: Conceptualization, Methodology, Software, Formal analysis, Investigation, Writing – original draft, Writing – review & editing, Visualization, Funding acquisition. **Kai Härkönen:** Methodology, Investigation, Writing – review & editing. **Petra Ilvonen:** Investigation. **Saara Laitinen:** Writing – review & editing, Supervision, Project administration, Funding acquisition. **Tapani Viitala:** Conceptualization, Methodology, Writing – review & editing, Supervision, Project administration, Funding acquisition.

Data availability

Data will be made available on request.

Acknowledgments

The authors thank EV Core Facility at the University of Helsinki. Karri Aalto and Aukusti Alanko are thanked for technical assistance. Funding for the work was provided by EVE Consortium (Business Finland 2346/31/2019). P.P. also acknowledges a personal grant from Alfred Kordelin Foundation (Grant No. 190242).

Appendix A. Supplementary data

Supplementary material related to this article can be found online at https://doi.org/10.1016/j.colsurfa.2022.130015.

References

[1] Z. Wang, F. Schmidt, Y. Weisblum, F. Muecksch, C.O. Barnes, S. Finkin, D. Schaefer-Babajew, M. Cipolla, C. Gaebler, J.A. Lieberman, T.Y. Oliveira, Z. Yang, M.E. Abernathy, K.E. Huey-Tubman, A. Hurley, M. Turroja, K.A. West, K. Gordon, K.G. Millard, V. Ramos, J. Da Silva, J. Xu, R.A. Colbert, R. Patel, J. Dizon, C. Unson-O'Brien, I. Shimeliovich, A. Gazumyan, M. Caskey, P.J. Bjorkman, R. Casellas, T. Hatziioannou, P.D. Bieniasz, M.C. Nussenzweig, mRNA vaccine-elicited antibodies to SARS-CoV-2 and circulating variants, Nature 592 (7855) (2021) 616–622, http://dx.doi.org/10.1038/s41586-021-03324-6.

[2] J.J. Rennick, A.P. Johnston, R.G. Parton, Key principles and methods for studying the endocytosis of biological and nanoparticle therapeutics, Nat. Nanotechnol. 16 (3) (2021) 266–276, http://dx.doi.org/10.1038/s41565-021-00858-8.

[3] K.A. Dawson, Y. Yan, Current understanding of biological identity at the nanoscale and future prospects, Nat. Nanotechnol. 16 (3) (2021) 229–242, http://dx.doi.org/10.1038/s41565-021-00860-0.

[4] A. Kapara, V. Brunton, D. Graham, K. Faulds, Investigation of cellular uptake mechanism of functionalised gold nanoparticles into breast cancer using SERS, Chem. Sci. 11 (22) (2020) 5819–5829, http://dx.doi.org/10.1039/d0sc01255f.

[5] D.L. Rupert, C. Lässer, M. Eldh, S. Block, V.P. Zhdanov, J.O. Lotvall, M. Bally, F. Höök, Determination of exosome concentration in solution using surface plasmon resonance spectroscopy, Anal. Chem. 86 (12) (2014) 5929–5936, http://dx.doi.org/10.1021/ac500931f.

[6] D.L.M. Rupert, G.V. Shelke, G. Emilsson, V. Claudio, S. Block, C. Lässer, A. Dahlin, J.O. Lötvall, M. Bally, V.P. Zhdanov, F. Höök, Dual-wavelength surface plasmon resonance for determining the size and concentration of sub-populations of extracellular vesicles, Anal. Chem. 88 (20) (2016) 9980–9988, http://dx.doi.org/10.1021/acs.analchem.6b01860.

[7] T. Suutari, T. Silen, D. Şen Karaman, H. Saari, D. Desai, E. Kerkelä, S. Laitinen, M. Hanzlikova, J.M. Rosenholm, M. Yliperttula, T. Viitala, Real-time label-free monitoring of nanoparticle cell uptake, Small 12 (45) (2016) 6289–6300, http://dx.doi.org/10.1002/smll.201601815.

[8] D.L. Rupert, M. Mapar, G.V. Shelke, K. Norling, M. Elmeskog, J.O. Lötvall, S. Block, M. Bally, B. Agnarsson, F. Höök, Effective refractive index and lipid content of extracellular vesicles revealed using optical waveguide scattering and fluorescence microscopy, Langmuir 34 (29) (2018) 8522–8531, http://dx.doi.org/10.1021/acs.langmuir.7b04214.

[9] F. Wang, B. Chen, B. Yan, Y. Yin, L. Hu, Y. Liang, M. Song, G. Jiang, Scattered light imaging enables real-time monitoring of label-free nanoparticles and fluorescent biomolecules in live cells, J. Am. Chem. Soc. 141 (36) (2019) 14043–14047, http://dx.doi.org/10.1021/jacs.9b05894.

[10] G.B. Adkins, E. Sun, R. Coreas, W. Zhong, Asymmetrical flow field flow fractionation coupled to nanoparticle tracking analysis for rapid online characterization of nanomaterials, Anal. Chem. 92 (10) (2020) 7071–7078, http://dx.doi.org/10.1021/acs.analchem.0c00406.

[11] Y. Dai, S. Bai, C. Hu, K. Chu, B. Shen, Z.J. Smith, Combined morpho-chemical profiling of individual extracellular vesicles and functional nanoparticles without labels, Anal. Chem. 92 (7) (2020) 5585–5594, http://dx.doi.org/10.1021/acs.analchem.0c00607.

[12] L. Rodriguez-Lorenzo, K. Fytianos, F. Blank, C. Von Garnier, B. Rothen-Rutishauser, A. Petri-Fink, Fluorescence-encoded gold nanoparticles: Library design and modulation of cellular uptake into dendritic cells, Small 10 (7) (2014) 1341–1350, http://dx.doi.org/10.1002/smll.201302889.

[13] A. Shehzad, S.U. Islam, R. Shahzad, S. Khan, Y.S. Lee, Extracellular vesicles in cancer diagnostics and therapeutics, Pharmacol. Ther. 223 (2021) 107806, http://dx.doi.org/10.1016/j.pharmthera.2021.107806.

[14] R.C. de Abreu, H. Fernandes, P.A. da Costa Martins, S. Sahoo, C. Emanueli, L. Ferreira, Native and bioengineered extracellular vesicles for cardiovascular therapeutics, Nat. Rev. Cardiol. 17 (11) (2020) 685–697, http://dx.doi.org/10.1038/s41569-020-0389-5.

[15] M. Palviainen, M. Saraswat, Z. Varga, D. Kitka, M. Neuvonen, M. Puhka, S. Joenväärä, R. Renkonen, R. Nieuwland, M. Takatalo, P.R. Siljander, Extracellular vesicles from human plasma and serum are carriers of extravesicular cargo—Implications for biomarker discovery, PLoS One 15 (8) (2020) e0236439, http://dx.doi.org/10.1371/journal.pone.0236439,

[16] E. Laurén, F. Tigistu-Sahle, S. Valkonen, M. Westberg, A. Valkeajärvi, J. Eronen, P. Siljander, V. Pettilä, R. Käkelä, S. Laitinen, E. Kerkelä, Phospholipid composition of packed red blood cells and that of extracellular vesicles show a high resemblance and stability during storage, Biochim. Biophys. Acta - Mol. Cell Biol. Lipids 1863 (1) (2018) 1–8, http://dx.doi.org/10.1016/j.bbalip.2017.09.012.

[17] R.L. Pinals, L. Chio, F. Ledesma, M.P. Landry, Engineering at the nano-bio interface: Harnessing the protein corona towards nanoparticle design and function, Analyst 145 (15) (2020) 5090–5112, http://dx.doi.org/10.1039/d0an00633e.

[18] S.K. Vashist, C.K. Dixit, B.D. MacCraith, R. O'Kennedy, Effect of antibody immobilization strategies on the analytical performance of a surface plasmon resonance-based immunoassay, Analyst 136 (21) (2011) 4431–4436, http://dx.doi.org/10.1039/c1an15325k.

[19] K. Salimi, D.D. Usta, A. Koçer, E. Çelik, A. Tuncel, Protein A and protein A/G coupled magnetic SiO2 microspheres for affinity purification of immunoglobulin G, Int. J. Biol. Macromol. 111 (2018) 178–185, http://dx.doi.org/10.1016/j.ijbiomac.2018.01.019.

[20] S. Liu, E. Haller, J. Horak, M. Brandstetter, T. Heuser, M. Lämmerhofer, Protein A- and protein G-gold nanoparticle bioconjugates as nano-immunoaffinity platform for human IgG depletion in plasma and antibody extraction from cell culture supernatant, Talanta 194 (2019) 664–672, http://dx.doi.org/10.1016/j.talanta.2018.10.079.

[21] A.H. Schmid, S.E. Stanca, M.S. Thakur, K.R. Thampi, C.R. Suri, Site-directed antibody immobilization on gold substrate for surface plasmon resonance sensors, Sensors Actuators, B Chem. 113 (1) (2006) 297–303, http://dx.doi.org/10.1016/j.snb.2005.03.018.

[22] M.L. Jeong, K.P. Hyun, Y. Jung, K.K. Jin, O.J. Sun, H.C. Bong, Direct immobilization of protein g variants with various numbers of cysteine residues on a gold surface, Anal. Chem. 79 (7) (2007) 2680–2687, http://dx.doi.org/10.1021/ac0619231.

[23] E. De Juan-Franco, A. Caruz, J.R. Pedrajas, L.M. Lechuga, Site-directed antibody immobilization using a protein A-gold binding domain fusion protein for enhanced SPR immunosensing, Analyst 138 (7) (2013) 2023–2031, http://dx.doi.org/10.1039/c3an36498d.

[24] M. Eliasson, A. Olsson, E. Palmcrantz, K. Wiberg, M. Inganäs, B. Guss, M. Lindberg, M. Uhlén, Chimeric IgG-binding receptors engineered from staphylococcal protein a and streptococcal protein G, J. Biol. Chem. 263 (9) (1988) 4323–4327, http://dx.doi.org/10.1016/s0021-9258(18)68928-8.

[25] C. Capasso, M. Hirvinen, M. Garofalo, D. Romaniuk, L. Kuryk, T. Sarvela, A. Vitale, M. Antopolsky, A. Magarkar, T. Viitala, T. Suutari, A. Bunker, M. Yliperttula, A. Urtti, V. Cerullo, Oncolytic adenoviruses coated with MHC-I tumor epitopes increase the antitumor immunity and efficacy against melanoma, Oncoimmunology 5 (4) (2016) e1105429, http://dx.doi.org/10.1080/2162402X.2015.1105429.

[26] P.K. Jain, X. Huang, I.H. El-Sayed, M.A. El-Sayed, Review of some interesting surface plasmon resonance-enhanced properties of noble metal nanoparticles and their applications to biosystems, Plasmonics 2 (3) (2007) 107–118, http://dx.doi.org/10.1007/s11468-007-9031-1.

[27] B. Taskinen, D. Zauner, S.I. Lehtonen, M. Koskinen, C. Thomson, N. Kähkönen, S. Kukkurainen, J.A. Määttä, T.O. Ihalainen, M.S. Kulomaa, H.J. Gruber, V.P. Hytönen, Switchavidin: Reversible biotin-avidin-biotin bridges with high affinity and specificity, Bioconjug. Chem. 25 (12) (2014) 2233–2243, http://dx.doi.org/10.1021/bc500462w.

[28] S. Valkonen, E. van der Pol, A. Böing, Y. Yuana, M. Yliperttula, R. Nieuwland, S. Laitinen, P.R. Siljander, Biological reference materials for extracellular vesicle studies, Eur. J. Pharm. Sci. 98 (2017) 4–16, http://dx.doi.org/10.1016/j.ejps.2016.09.008.

[29] S. Suherman, K. Morita, T. Kawaguchi, Surface plasmon resonance for detecting clenbuterol: Influence of monolayer structure, Appl. Surf. Sci. 332 (2015) 229–236, http://dx.doi.org/10.1016/j.apsusc.2015.01.169.

[30] K. Norling, M. Sjöberg, M. Bally, V.P. Zhdanov, N. Parveen, F. Höök, Dissimilar deformation of fluid-and gel-phase liposomes upon multivalent interaction with cell membrane mimics revealed using dual-wavelength surface plasmon resonance, Langmuir 38 (8) (2022) 2550–2560, http://dx.doi.org/10.1021/acs.langmuir.1c03096.

[31] E. van der Pol, A.G. Hoekstra, A. Sturk, C. Otto, T.G. Van Leeuwen, R. Nieuwland, Optical and non-optical methods for detection and characterization of microparticles and exosomes, J. Thromb. Haemost. 8 (12) (2010) 2596–2607, http://dx.doi.org/10.1111/j.1538-7836.2010.04074.x.

[32] A. Koponen, E. Kerkelä, T. Rojalin, E. Lázaro-Ibáñez, T. Suutari, H.O. Saari, P. Siljander, M. Yliperttula, S. Laitinen, T. Viitala, Label-free characterization and real-time monitoring of cell uptake of extracellular vesicles, Biosens. Bioelectron. 168 (August) (2020) http://dx.doi.org/10.1016/j.bios.2020.112510.